Statistical study of heavy ion energization in the near-Earth magnetotail using a cross-correlation approach: Magnetospheric Multiscale (MMS) Observations

Romina Nikoukar[1], Ian J. Cohen[1], Barry Mauk[1], Roman Garcia Gomez[2], Xun Zhu[1], Stephen A. Fuselier[2,3], Sam T. Bingham[1†], and Drew L. Turner[1]

[1] The Johns Hopkins University Applied Physics Laboratory, Laurel, MD, United States

[2]Southwest Research Institute, San Antonio, TX, United States

[3]The University of Texas at San Antonio, San Antonio, TX, United States

[†]Deceased

Corresponding author: Romina Nikoukar (romina.nikoukar@jhuapl.edu)

Key Points (to be completed later):

- We exercise "energy-cross-correlation" techniques for various magnetotail conditions to discern ion charge state and energization processes.
- Magnetotail dynamics are coherent enough to allow for consistent coarse determination of the charge state of energetic heavy ions (O^{6+} and He^{++}).
- Magnetotail dynamics are too complex for the distinct and regular determination of adiabatic versus non-adiabatic energization for energetic heavy ions.

Abstract

We present a statistical study of energetic heavy ion acceleration in the near-Earth magnetotail using observations from the Energetic Ion Spectrometer (EIS) onboard the Magnetospheric Multiscale (MMS) spacecraft. Although the EIS instrument does not measure ion charge state directly, we have inferred the dominant charge state of the suprathermal heavy ions (i.e., ~60-1000 keV He and C-N-O), using a previously-developed correlation analysis of the time-dependent flux response between different energy channels of different ion species. For specific events we have also distinguished adiabatic (charge-dependent) energization from non-adiabatic (mass-dependent) energization. This work uses observations from the MMS "Bursty Bulk Flows (BBF) Campaign" in August 2016, when high-energy-resolution "burst"-mode data are more frequently available, to examine the relative occurrence of adiabatic energization versus preferential energization of heavy ions. The results of this study demonstrate the utility and limitations of the cross-correlation technique that was applied. We find that the technique is consistently able to discern coarse charge states for heavy ions such as $O^{+/6+}$, $He^{+/++}$ (i.e., ionospheric versus solar wind sources), but that the more subtle job of uniquely determining adiabatic versus non-adiabatic behaviors for the ionospheric component (O^{+}) is only sometimes achievable. The dynamics of Earth's magnetotail are apparently too complex and variable to consistently accommodate our simple assumption for adiabatic behavior of energy/charge-ordered transport from a common source of particles.

Plain Language Summary

Space environments of magnetized planets, called "magnetospheres", trap and accelerate energetic ions (ionized atoms) and electrons. At Earth, these particles come from two different sources, the "ionosphere" of charged gases at the top of Earth's atmosphere, and ionized gases comprising the solar wind emanating from the Sun and enveloping Earth's magnetosphere. Understanding the structure and dynamics of Earth's magnetosphere requires that we determine the sources of the particles within it. The charge states of the oxygen and helium ions provide good indicators of their source: low charge states (e.g., O^{+} and He^{+}) indicate ionospheric sources, and high charge states (e.g., O^{6+} and He^{++}) indicate a solar wind source. However, measuring the charge state is difficult; most instruments flown within Earth's magnetosphere are unable to make this determination. Previously, an analysis technique called "energy cross correlation" has allowed us to infer the charge states and also determine how the particles are energized. Here we use this technique for a broad range of conditions to determine the strengths and limitations of this technique. The results demonstrate that the technique is very good at distinguishing the charge state of heavy ions like oxygen, but only sometimes allows us to determine the mechanisms of energization.

1 Introduction

Energetic ions (tens to hundreds of keV) in the ring current and nightside plasma sheet make a significant contribution to energy density and plasma pressure in the magnetosphere (e.g., Williams, 2015). They also play a key role in the plasma and field dynamics in the inner magnetosphere (e.g., Kozyra & Liemohn, 2003; Ebihara & Ejiri, 2003). The major ion species in the magnetosphere are protons, oxygen, and helium (e.g., Young et al., 1982; Welling et al., 2015). Protons originate from both the solar wind and ionosphere. Ionospheric outflow also contains singly-charged oxygen (and to a lesser degree He^{+}, N^{+}, O^{++}, and molecular ions) while multiply-charged oxygen ($O^{\geq 3}$) and carbon ($C^{\geq 3}$) originate from the solar wind (e.g., Shelley et

al., 1972; Gloeckler, & Hamilton, 1987; Kermser et al., 1985, 1987; Moore et al., 2001; Allen et al., 2016; Jordanova et al., 2020). This charge dependence allows for heavy ions to serve as tracers of ionospheric-originating plasma versus solar wind-originating plasma (e.g., Allen et al., 2016). Furthermore, because different ion species with different charge states can experience energization processes with a wide range of different spatial and temporal scales, the *mass-per-charge* (*m/q*) values in the magnetosphere have been used as a tracer to study the origin, acceleration, and energization of magnetospheric plasma (e.g., Balsiger et al., 1980).

In the absence of composition and/or charge-state measurements, it is common to assume that either magnetospheric dynamics are predominantly controlled by protons and/or heavy ions are singly charged (e.g., Ziegler et al., 2010, Mauk, 2013, Blake et al., 2016; Cohen et al., 2017). However, both of these assumptions may result in widely different interpretations of ion heating and energization processes (e.g., charge state energization vs. mass-dependent energization). In order to properly understand magnetospheric dynamics - including energization, transport, injection, and loss processes of energetic particles - it is important to distinguish both composition and charge state.

Over the past decades, many satellite observations and modeling studies have focused on storm-time and substorm evolution of ion composition, hinting at various heavy ion energization processes/mechanisms, charge-dependent and/or mass-dependent, in the magnetosphere. It is shown that singly-charged oxygen ions can have a significant contribution to the pressure of the plasma sheet and ring current during geomagnetic activity while the protons typically dominate the pressure during quiet periods (e.g., Young et al., 1982; Hamilton et al., 1988; Kistler et al., 1989; Roeder et al., 1996; Daglis, 1977; Nosé et al., 2001; Fok et al., 2006; Keika et al., 2006; 2010, 2013; Gkioulidou et al., 2016; Mouikis et al., 2019). Although various adiabatic and non-adiabatic energization processes have been proposed, the nature and prevalence of preferential O^+ ion enhancements and the dominant mechanisms are still under debate. The major likely processes include adiabatic (i.e., charge state-dependent) transport from the plasma sheet under prolonged strong convection (e.g., Kronberg et al., 2014), impulsive adiabatic transport associated with fast plasma flows from the plasma sheet and magnetic field dipolarization, and local non-adiabatic (i.e., revealing itself as mass-dependent) acceleration in the plasma sheet and inner magnetosphere (Keika et al., 2013, 2018; Fu et al., 2020; and references therein).

For guiding-center adiabatic behavior, ions with different charge states have the same drift trajectories and charge-state-dependent energization, irrespective of their mass. Such energy-per-charge ordering of the observed spectra is reported in various studies (e.g., Mobius et al., 1987, Kistler et al., 1989, 1990; Cohen et al., 2017; and references therein). However, there are many hypothesized conditions where non-adiabatic, mass-dependent acceleration is expected. Test particle trajectories in magnetohydrodynamic (MHD) field simulations of dipolarizations by Birn et al. (2013, 2014) have shown non-adiabatic acceleration of ions close to the reconnection site where magnetic spatial and/or temporal scales are smaller than ion gyroradii and/or gyro-frequencies. Ion trapping within modeled magnetic islands and other local non-adiabatic processes have also been modeled for dipolarization events (Ukhorskiy et al., 2017, 2018). During dynamic events, O^+ is often expected to behave non-adiabatically compared to H^+ because of its longer gyroperiods relative to the time scales of the dynamics. This behavior could lead to preferential energization of O^+ associated with impulsive electric fields of several types of dynamic features (e.g., Keika et al., 2013; and references therein). Such features include: (1) magnetic field dipolarization (e.g., Delcourt et al., 1994, Sanchez et al., 1993, Wygant et al.,

1998), (2) magnetic field reconfiguration and/or the leading edge of a fast earthward propagating plasma structure such as a bursty bulk flow (e.g., Nakamura et al., 2003, Sergeev et al., 2009), (3) Pc1-2 magnetic field fluctuations during dipolarization (e.g., Ono et al., 2009, Nosé et al., 2010), (4) resonant interactions with electromagnetic ion cyclotron waves (e.g., Thorne & Horne, 1997), and (5) ultralow-frequency waves (e.g., Yang et al., 2011). However, to discern such non-adiabatic behaviors, we must understand the charge states of the ions involved. Specifically adiabatic acceleration of multiply-charged heavy ions of solar wind origin above ~150 keV injected Earthward from the magnetotail and the subsequent energy per charge (*E/q*) ordering has been suggested recently by multiple authors (e.g., Cohen et al., 2017; Bingham et al., 2020, 2021; Birn et al., 2021). In this case, He^{++} and O^{6+} would acquire two and six times more energy than protons, respectively.

To address adiabatic versus non-adiabatic energization, one needs to discriminate suprathermal ions originating from the solar wind from ionospheric heavy ions produced during magnetospheric ion enhancements. Using the high-energy composition observations from the Radiation Belt Storm Probes Ion Composition Experiment (RBSPICE) instrument (Mitchell et al., 2013) onboard the Van Allen Probes at radial distances < 5.8 R_E, Mitchell et al. (2018) first introduced a technique using cross correlation analysis of the time-varying intensities of helium and oxygen ions to deduce their charge state. Bingham et al. (2020) applied this technique to data from the Energetic Ion Spectrometer (EIS) instrument (Mauk et al., 2016) onboard the Magnetospheric Multiscale (MMS) mission for more distant regions and concluded that the fluxes were ordered by energy-per-charge (*E/q*) for three specific events featuring adiabatic energization. Later, Bingham et al. (2021) used this technique to reveal apparent non-adiabatic acceleration during one event using MMS/EIS data.

In this work, we expand on these previous studies to conduct a multi-case and statistical study of heavy ion energization in the near-Earth magnetotail using MMS observations to determine the utility, efficacy, and limitations of the cross-correlation technique in determining the occurrence frequency of adiabatic (i.e., charge-dependent) and non-adiabatic (i.e., mass-dependent) energization of heavy ions. The central issue is whether the magnetotail consistently behaves in the fashion that is assumed in the application of the technique. In Section 2, we introduce the instrumentation. In Section 3, we discuss the event selection and methodology, showcase our analysis results for a few events, and present the results of our statistical study. Section 4 provides a discussion and conclusion.

2 Instrumentation

The MMS mission (Burch et al., 2016), launched on 13 March 2015, consists of four identically-instrumented spacecraft flying in highly elliptical, near-equatorial Earth orbits in a tight tetrahedral spacing of tens to hundreds of km. The orbits along with a comprehensive set of particles and field instruments allow for observations of magnetosphere dynamics at electron scales at various radial distances. In this study, we use observations from the instrumentation onboard MMS spacecraft as follows.

The EIS instrument is one of two sensor types of the Energetic Particle Detector (EPD) investigation (Mauk et al., 2016) and uses microchannel plates and solid-state detectors to measure energetic ion energy, pitch angle, and elemental compositional distributions for protons (~20 keV to 1 MeV), helium (~60 keV to 1 MeV), and oxygen (130 keV to 1 MeV) using an

"energy by time-of-flight" (ExTOF) technique for heavy ions and higher energy protons and a microchannel plate (MCP) "pulse-height by time-of-flight" (PHxTOF) technique for the lower energy protons in six different views in a plane. We note that EIS does not distinguish between carbon, nitrogen, and oxygen (CNO) nor does it distinguish charge state.

The Hot Plasma Composition Analyzer (HPCA; Young et al., 2016) and the Fast Plasma Investigation (FPI; Pollock et al., 2016) provide ion moments and velocity distributions. HPCA is a time-of-flight (TOF) mass spectrometer designed to measure energy, angle, and velocity distributions for different ion species with various charge states (e.g., H^+, He^{++}, He^+, O^+, O^{++}) in a lower energy range between a few eV and ~40 keV/q. In our analysis, in addition to the estimated ion flow speed from HPCA, we use burst-mode HPCA composition (i.e., charge state) data to either confirm or reject the presence of O^+ and/or He^+ for our identified events. The Fluxgate Magnetometer (FGM) instrument (Russell et al., 2016) provides the vector magnetic field on MMS. The solar wind and geomagnetic index data are obtained from the NASA OMNI dataset (King & Papitashvili, 2005).

3 Analysis and Results

3.1 Event Selection

The statistical study presented here includes MMS observations of energetic particle enhancements during substorm activity in August 2016 when the MMS "Bursty Bulk Flow (BBF) Campaign" was conducted during Phase 1x of the mission (Fuselier et al., 2016). Consequently, a higher percentage of burst-mode data was available as compared to other phases of the mission. EIS burst data is sampled at the full sectoring cadence of the instruments (i.e., ~2/3-s accumulation) and has a $\Delta E/E$ of 10%, compared to 35% during typical "survey-mode" data acquisition. At burst resolution, there are up to 73 channels of various combinations of ExTOF-measured species and energy for each look direction.

For each species (H^+, He^{n+}, O^{n+}), we use spin-averaged, omni-directional fluxes versus energy where the data is combined over the six different EIS telescopes (or look directions). The temporal resolution is ~20 s in this case. Since the spatial separations of the four MMS spacecraft are small compared to the ion gyroradii, we combine the data from all the MMS spacecraft (except MMS1 for which no EIS ion data products are available during the "BBF Campaign") to improve statistical accuracy.

We identified a total of 32 events for study. For our selection of the events, we focused on time intervals for which the burst-mode data were available (lasting for at least eight minutes), and ion enhancement signatures were observed (visual inspecition). Because the FPI instrument did not operate during the August 2016 campaign, we used ion bulk flow speeds measured by HPCA.

3.2 Methodology

In this work, we employ the technique introduce by Mitchell et al. (2018) and used by Bingham et al. (2020, 2021). Specifically, we compute the Pearson cross-correlation coefficients for the time history of fluxes in different energy channels associated with different species (protons, helium, and oxygen), as follows

$$\rho_{X,Y} = \frac{\mathbb{E}[(X-\mu_X)(Y-\mu_Y)]}{\sigma_X \sigma_Y},$$

where $\mathbb{E}$ represents the expectation operator and μ_X, and σ_X note the average and standard variation of the species X timeseries, respectively. With this technique, a ridge of high cross-correlation between certain energy ranges for two different species can indicate the presence or absence of *E/q* ordering of the dynamics and can be used to infer the dominant heavy ion charge state during substorm-related energetic particle enhancements.

3.3 Multi-case Analysis Results

Here we present the results of the multi-case analysis using the cross-correlation technique to better understand the nature of dynamics of ion injection events during substorm activity and the efficacy of the technique. We showcase three example cases that feature three different behaviors in terms of adiabatic versus non-adiabatic energization of singly-charged oxygen ions.

3.3.1 Category 1 example: Adiabatic enhancement of helium and oxygen

The first example case that we present is for an energetic particle enhancement event between 07:00 and 07:40 UT on 20 August 2016. Figure 1 shows the solar wind conditions from OMNI data (Figures 1a-1d) and substorm auroral indices (*AE*, *AU*, *AL*) (Figure 1e) for 00:00-24:00 UT. The figure also shows MMS observations from 07:00-07:40 UT (Figures 1f-1j). The solar wind speed is relatively steady at ~325 km/s. The AE index varies from ~200 nT to ~500 nT, indicating moderate substorm activity. During this time, the MMS spacecraft were on the inbound portion of their orbit from ~9.4 R_E to ~8.8 R_E at a magnetic local time (MLT) of 21.6-21.8 hr. Figures 1f-1h show energy spectrograms of spin-averaged omnidirectional fluxes observed by EIS for 40-1000 keV protons (ExTOF product), 60-1000 keV helium, and 130-1000 keV oxygen ions, respectively. As explained in Section 2, we combine the EIS observations over all available spacecraft (MMS2-MMS4) because of their small separation compared to the ion gyro-scales. These spectrograms show enhancements of proton, helium, and oxygen ions during this time interval. Figures 1i-j show the FGM magnetic field and HPCA proton velocities from MMS2 in GSM coordinates. Since B_x is negative, $-B_x$ is plotted for better visualization of changes in the magnetic field components. Signatures of dipolarization accompanied by large flow speeds ($+V_x$ component) up to ~750 km/s are observed between 07:02-07:10 UT, entirely consistent with this being an energetic particle injection associated with a dipolarization of the local magnetotail (note increase in $+B_z$ with associated decrease in magnitude of B_x) and an earthward BBF.

The energy ranges of ion enhancements differ for different ion species (e.g., Mitchell et al., 2018; Bingham et al., 2020). Heavier ion enhancements are apparent at much higher energies (up to ~1 MeV) compared to protons for which enhancements happen up to ~350 keV. As previously mentioned, EIS does not measure charge state; therefore, if we were to assume that the heavy ions are singly-charged, extreme electric potentials would be required to energize ions to such high energies.

To determine charge state, we apply the cross-correlation methodology described in Section 3.2. Assuming that magnetospheric dynamics are controlled by energy-per-charge (i.e., guiding-center assumption), this method sheds light on the heavy ion charge state during this event. Figure 2 shows time series of the differential flux for EIS protons at 55 keV, 81 keV, and 120 keV energies and helium at 103 keV, 169 keV, and 244 keV. We note that time series of

helium are normalized on the y-axis relative to the proton time series to facilitate visualization. The time series are smoothed over 1 min. As a precursor to the more formal treatment to come, the coherency between the temporal variation of helium and protons fluxes for energies where the condition $E_{He} = 2 * E_H$ is roughly met is evident from these plots. This result indicates that the cross-correlation between such energy pairs is high (i.e., close to 1) for this event.

To formalize and confirm this conclusion, Figure 3a presents a table of cross-correlation coefficients of the pairs of time series of proton and helium differential fluxes for all EIS energy channels between 07:06-07:40 UT. We did not include the differential fluxes before 07:06 UT when high flows were observed in HPCA measurements because the Compton-Getting effect from high flows might distort the ion energies. In panel (a), the row and column headers list the geometric mean energy of each EIS proton and helium channel. The colored boxes note the cross correlation of fluxes between each respective pair of energy channels. We can think of time as going into the page, and the colored box identifing the cross-correlation coefficient between the time series associated with each pair of proton and helium energies. The coefficients are color-coded to note high (1) and low (0 or small negative) values in blue and red, respectively. The boxes with yellow outlines are added to guide the eyes to energy channel pairs for which either helium energies are closest or equal to proton energies (i.e., $E_{He} = E_{H^+}$, bottom diagonal line of yellow boxes) or twice the proton energies (i.e., $E_{He} = 2 * E_{H^+}$, top diagonal line of yellow boxes). These boxes signify where peak correlations would be expected if transport and energization were ordered by *E/q* for H^+ versus He^+ (bottom line of yellow boxes) or He^{++} (top line of yellow boxes).

In this table, we see a ridge of high cross-correlation coefficients along the top diagonal line of yellow boxes where $E_{He} = 2 * E_{H^+}$ indicating the presence of He^{++}. While the ridge is well focused along $E_{He} = 2 * E_{H^+}$ boxes for $E_{He} \gtrsim 200$ keV, it expands for lower energy channels. One reason behind this widening of the ridge could be the presence of both He^+ and He^{++}. Remember that HPCA can observe both singly-charged and doubly-charged helium at energies below ~40 keV/q (or ~ 80 keV total energy). Figure 3d shows the TOF spectrum from HPCA between 07:00 UT and 07:40 UT. Color illustrates the average flux observed by HPCA for a given bin. Each bin – i.e., the region between the solid-dashed lines - represents the respective TOF ranges for each ion species. The solid-dashed line pairs show the fast and slow TOF limits, respectively, for the species. As expected, helium fluxes are several orders of magnitude lower than proton fluxes; however, HPCA shows that He^{++} ions dominate by approximately an order of magnitude over those of He^+ at energies above ~1 keV. This significant He^{++} population likely explains the broadening of the high cross-correlation ridge for the lower EIS energy channels in Figure 3a.

Figure 3b shows the same cross-correlation table as Figure 3a, but between proton and oxygen energy channels. There are now three diagonal lines of boxes with yellow outlines corresponding to: $E_O = E_{H^+}$ (bottom line), $E_O = 2 * E_{H^+}$ (middle line), $E_O = 6 * E_{H^+}$ (top line). Two sets of high cross-correlations ridges are evident for this case, indicating two distinct oxygen populations. For the lower energy oxygen ($E \lesssim 300$ keV), the peak correlations fall along $E_O = E_{H^+}$. This association with H^+ suggests the presence of O^+ and its adiabatic acceleration, where *E/q* ordering of the dynamics is expected. The HPCA TOF spectrum confirms that there is a high flux of singly-charged oxygen but very little flux of doubly-charged oxygen. A second weak ridge of high correlations falls along $E_{O^+} = 6 * E_{H^+}$ energies although the ridge is much less coherent compared to those for $E_O = E_{H^+}$ in Figure 3b and $E_{He} = 2 * E_{H^+}$ in Figure 3a. This high

correlation ridge hints at the presence of an O^{6+} population at E ≳ 350 keV, which is again adiabatically energized in the near-Earth magnetotail. Previously-published events show a much stronger signal of O^{6+} (e. g., Mitchell et al., 2018; Bingham et al., 2020)

Figure 3c shows the same cross-correlation table as Figures 3a-b, but between helium and oxygen energy channels. The diagonal lines with yellow outlines now correspond to $E_O = \frac{1}{2} * E_{He}$, $E_O = E_{He}$, and $E_O = 3 * E_{He}$ (bottom, middle, and top lines, respectively). The ridge of highest cross-correlation falls along energy channels where $E_O = \frac{1}{2} * E_{He}$ (i.e., a 2:1 helium-to-oxygen charge state ratio, as would result from O^+ and He^{++} populations) while another ridge of relatively high correlations is observed along the energy channels where $E_O = 3 * E_{He}$ (i.e., a 1:3 helium-to-oxygen charge state ratio, as would result from O^{6+} and He^{++} populations). These results are in good agreement with the previously-discussed charge state populations determined from the correlation tables in Figures 3a and 3b, and further bolster the idea that the dynamics for this case are well ordered by *E/q*.

This event is an example of the first category of events - similar to ones noted by Bingham et al. (2020) - with energization largely ordered by *E/q* (i.e., suggesting adiabatic energization for both helium and oxygen species). Note that the helium-to-oxygen cross-correlation tables follow the general patterns observed in the proton-to-helium and proton-to-oxygen cross-correlation tables although the cross-correlation values are typically smaller. This decrease in cross-correlation coefficients might be due to the fact that the heavy ion fluxes are significantly lower compared to protons fluxes and hence lead to much higher uncertainties associated with the cross-correlation coefficients.

3.3.2 Category 2 example: Adiabatic enhancement of He^{++} and O^{6+} and apparent non-adiabatic enhancement of O^+

The second example case presented here is an enhancement event on 24 August 2016 between 06:45 UT and 08:40 UT. Figure 4a-4e shows the same OMNI data and auroral indices as Figure 1. In this time interval, the AE index varies between 200 nT and 400 nT. The solar wind speed is steady at about ~500 km/s. Figure 4f-4j show MMS observations from EIS, FGM, and HPCA with a format similar to Figure 1f-1j. The spacecraft are on their inbound orbit from ~8.9 R_E to ~7.3 R_E at MLT of 21.5-22.0 hr. The EIS data are again combined from MMS2-4. The FGM and HPCA are from MMS3. Signatures of dispersed injections can be seen at ~06:52 UT, 07:35 UT, 07:40 UT, and 07:45 UT accompanied by dipolarization of magnetic field. High speed (~600 km/s) plasma flows are observed at the beginning of the interval.

Figure 5 shows the tables for the cross-correlation coefficients between protons and helium (5a), protons and oxygen (5b), helium and oxygen (5c), and the HPCA TOF spectrum (5d). The format of diagonal lines with yellow outlines is similarly configured to those in Figure 3. The cross-correlation coefficients for this event are high along $E_{He} = 2 * E_{H^+}$ (Figure 5a), which is an indication of adiabatic energization of helium. It is uncertain why this ridge becomes slightly wider for helium energies between ~150 keV and ~275 keV. This cross-correlation table is rather similar to that of the previous example case for the event on 20 August 2016 in that the helium energization seems to follow *E/q* dynamics (i.e., adiabatic energization).

The cross-correlation tables between proton and oxygen (Figure 5b) and helium and oxygen (Figure 5c) show two distinct ridges of high correlations for low-energy oxygen (<300 keV) and high-energy oxygen (>300 keV) revealing two populations. Similar to Figures 3b-c, the higher-

energy (>300 keV) ridges lie very nicely across boxes with $E_O = 6 * E_{H^+}$ (Figure 5b) and $E_O = 3 * E_{He}$ (Figure 5c). Given the clear dominance of He^{++} in this event, this alignment denotes the presence of O^{6+} ions of solar wind origin and their adiabatic energization.

However, for the lower-energy (<300 keV) oxygen, the high cross-correlation ridge falls between the lines expected for $E_O = E_{H^+}$ and $E_O = 2 * E_{H^+}$ in Figure 5b and $E_O = 1/2 * E_{He}$ and $E_O = E_{He}$ in Figure 5c; given again the clear dominance of He^{++} in this event this suggests a population of either O^+ and/or O^{++}. This is in contrast to previous results from Mitchell et al. (2018) and Bingham et al. (2020) – as well as those in Figures 3b-c - where we had the cross-correlations suggest the clear adiabatic energization of singly-charged oxygen. To determine if this offset is due to the presence of O^{++} (i.e., a mixed population of O^+ and O^{++}) or preferential energization of O^+, we examine the HPCA TOF spectrum between 6:45 UT and 8:40 UT (Figure 5d). This plot reveals higher fluxes (approximately several orders of magnitude) for O^+ compared to O^{++} at energies up to 40 keV/q. The clear lack of significant O^{++} in the HPCA measurement makes it highly unlikely that the presence of O^{++} can explain the position of the correlation ridge. This event is also consistent with typical conditions when O^{++} fluxes have historically been found to be much lower compared to O^+ intensities (e.g., Kremser et al., 1987). Based on these observations, we conclude that there is a true displacement of the high cross-correlation ridge from the position expected for *E/q*-ordered (i.e., adiabatic) energization ($E_O = E_{H^+}$).

This example case represents a category that is more similar to the event studied by Bingham et al. (2021) where an offset in peak correlations for protons and oxygen was also concluded to be indicative of a non-adiabatic (preferential) energization of singly-charged oxygen ions. This might represent instances of pick-up energization, as also discussed in Bingham et al. (2021)

3.3.3 Category 3 example: Non-deterministic case of adiabatic versus non-adiabatic behavior of O^+

The final example case presented here is from 9:40 UT - 10:10 UT on 6 August 2016. Figure 6 shows the OMNI parameters (6a-d), auroral indices (6e), and MMS observations of EIS energy spectra (6f-h), FGM magnetic field (i) and HPCA ion flow (j) with a similar format to Figures 1 and 4. The MMS spacecraft are on an inbound trajectory at radial distances from 8.4 to 7.8 R_E. The AE index reaches up to ~1500 nT in this short interval indicating strong substorm activity. Signatures of dispersionless and dispersed injections associated with magnetic field dipolarizations are observed throughout this time interval as well. Since there are not any strong BBFs associated with the ion enhancements, it is likely that the dipolarization occurred over a broad range of MLT across the nightside and was remotely observed by MMS.

Figure 7a-c shows the tables of cross-correlation between energy channels for different species similar to those in Figures 3 and 5. Figure 7a again shows the likely dominance of He^{++} at energies $E_{He} \gtrsim 200$ keV as seen in the previous example cases. However, like example case 1 (Section 3.3.1; Figure 3a), the ridge is wider at lower energies. Inspection of the HPCA TOF spectrum for this time period (Figure 7d) shows that He^+ ion fluxes are not too different from He^{++} at energies less than 40 keV/q, suggesting that the widening of the cross-correlation ridge might be the result of increased He^+ fluxes.

However, unlike the previous cases, the cross-correlation coefficient tables for protons-vs.-oxygen (Figure 7b) and helium-vs.-oxygen (Figure 7c) for this event are much less coherent. In

Figure 7b, we can still observe higher correlations along $E_O = 6 * E_{H^+}$ for oxygen ions with energies >300 keV although the ridge of high correlation looks much broader for energies $E_O <$ 500 keV. The correlation coefficients are relatively high > 0.6 in flattened ridges for both i) 133 keV $< E_O <$ 175 keV and 55 keV $< E_H <$ 93 keV – i.e., at $E_O = 2 * E_{H^+}$, and ii) 228 keV $< E_H <$ 382 keV and 210 keV $< E_O <$ 390 keV (i.e., along the $E_O = E_{H^+}$ line). The HPCA TOF spectrum for this time interval in Figure 7d does not show a significant O^{++} population. Similarly, the cross-correlation table for helium-versus-oxygen (Figure 7c) has a large spread between at $E_O \lesssim$175 keV and 61 keV $\lesssim E_{He} \lesssim$191 keV between the lines expected for $E_O = 3 * E_{He}$ and $E_O = E_{He}$. Yet another ridge of high correlation is observed along $E_O = 3 * E_{He}$ at higher energies ($E_O \gtrsim$ 400 keV) similar to previous example cases with a clear O^{6+} population of solar wind origin.

This example case is representative of the third and final category of events for which the cross-correlation technique cannot definitively address the issue of ordering with respect to *E/q* – i.e., determination between adiabatic versus non-adiabatic energization. Considering that O^+ ions form the main population for oxygen ions at energies lower than ~300 keV, and that this event occurs during strong substorm activity, we speculate that multiple energization mechanisms are at play for the oxygen ions other than simple pickup energization; hence the table of cross-correlations is not as clearly organized as for previous example cases. This observation is presumably more evident for oxygen compared to helium because of its larger gyroradius and longer gyroperiod.

3.4 Statistical study

During MMS's BBF Campaign in August 2016, we identified thirty-two (32) enhancement events for which burst-mode data were available over at least an eight-minute period. To put the events into context, Figure 8 presents a) the distribution of the enhancement events in terms of maximum substorm activity (i.e., auroral electrojet index, AE) for the duration of the events, b) the event distribution in MLT, and c) the event distribution in radial distance. Except for one event, the identified enhancement events occurred during weak-to-moderate or strong substorm activity. The events all occurred at distances of either ~8-9 R_E or 11-12 R_E (the apogee of the MMS spacecraft was ~12 R_E for the BBF Campaign) but because they were selected from only a single month of MMS data during Phase 1x (Fuselier et al., 2016), they all occurred in the pre-midnight sector, approximately unfirmly distributed from 20-23 hr MLT. These events were sorted into three categories represented by the example cases summarized in Section 3.3.

Here, we list the major findings of the statistical analysis of these events:

- For all 32 events, the cross-correlation coefficients show ridges of high correlation along $E_{He} = 2 * E_{H^+}$ This signifies the presence of He^{++} and the adiabatic energization of helium ions. At times, the ridge becomes wider, especially for lower energy helium ions. Based on lower-energy HPCA measurements, we attribute this wider spread to the presence of He^+.
- 28 (88%) events show clear separation between low- and high-charge states for oxygen ions (O^+ and O^{6+}). In other words, the cross-correlation coefficients for proton-versus-oxygen channels display two separate ridges of high correlations for low-energy and high-energy oxygen. The technique is generally successful in separating high-charge states from low-charge states.

- In general, the cross-correlation coefficients for helium-versus-oxygen channels look less structured with the boundaries for high cross correlation ridges less clear compared to those of between protons and oxygen channels.
- Eight (25% of all events) show clear *E/q*-ordered (adiabatic) behavior and thirteen (41% of all events) show evidence of non-adiabatic behavior.
- Eleven events (11% of all events) yielded inconclusive cross-correlation tables that do not show clear structures for high cross-correlation ridges between protons and singly charged oxygen ions.
- The high cross-correlation ridges around either ~8-9 R_E or 11-12 R_E observed for $E_O >$ 300 keV were organized along either $E_O = 6 * E_{H^+}$ for protons-versus-oxygen channels, or $E_O = 3 * E_{He}$ for helium-versus-oxygen channels. This organization confirms that the higher-energy oxygen ions are mainly O^{6+} of solar wind origin, as reported in previous studies (e.g., Bingham et al., 2020, Birn et al., 2021; Cohen et al., 2017).

Figure 9 presents the distribution of the enhancement events in terms of substorm activity for the three different event categories: adiabatic, non-adiabatic, and non-deterministic. The adiabatic energization of O^+ has a nearly uniform distribution in terms of substorm strength (i.e., AE index). However, the distribution is skewed towards stronger substorm activity for non-adiabatic energization and inconclusive energization events. This result is expected since strong and transient flows during strong substorm activity make it more likely that either the first or second adiabatic invariants are broken for oxygen ions due to their larger gyroradii and longer gyroperiods.

4 Discussion and Conclusion

In this work, we presented a statistical study of the application of the cross-correlation technique on MMS/EIS observations and its efficacy to infer the charge state and aspects of acceleration associated with various ion species. As previously mentioned, EIS does not measure ion charge state, and a simple assumption that all ions are singly-charged, while may perhaps be valid for lower energies, can lead to vastly different interpretations of ion energization within the magnetosphere.

The three example cases discussed in Section 3.3 were presented as representative of three event categories:

1) *E/q*-ordered events, assumed to represent adiabatic dynamics (8 events, 25%)
2) Well-formed correlation traces that show evidence of non-*E/q* ordering, assumed to represent non-adiabatic energization of singly-charged oxygen (13 events, 41%)
3) The cross-correlation coefficients tables were coarsely conclusive with regard to charge state, but nonconclusive (indeterminant) in terms of energization behavior (11 events, 34%)

In the work of Bingham et al. (2021), a preliminary and relatively simplistic approach was used to interpret an event in category 2 above in terms of a so-called “pick-up” process, which occurs when a very strong electric field is turned on at a rate much faster than the ion gyroperiod. Figure 10 shows an idealized calculation based on this idea. One interpretation of the correlation shift observed by Bingham et al. (2021) was based on the mean (blue) trace shown. However, it is recognized that the final energization depends on the initial gyrophase of the O^+ ion; the orange and grey lines show the maximum and minimum energies achieved by the distribution of ions with a distribution of initial gyrophases. And so, the initial analysis by Bingham et al.

(2021) ignored the relatively broad range of energy shifts that could be generated by such a process.

The results of the present paper also lead us to reconsider other aspects of the assumptions that went into the initial analysis of the apparent non-adiabatic behavior by Bingham et al. (2021). Figure 11 shows three different theoretical scenarios that may, or may not, apply for the interpretation of our correlations.

In Scenario #1 (Figure 11a), injections of protons and oxygen ions occur far from the spacecraft. For this scenario, the ions would reach the spacecraft by magnetic drifts ordered by *E/q*. In this case, even if non-adiabatic acceleration is responsible for generating an enhancement of higher-energy oxygen (compared to protons), their drift to the spacecraft is ordered by *E/q* once they are injected and thus leave no way for us to determine the adiabatic energization as H^+ and O^+ ions at a given energy will arrive at the spacecraft at roughly the same time. In other words, in this scenario, it is not possible to say if any observed *E/q* ordering is a result of the acceleration or the transport processes.

For Scenario #2 (Figure 11b), injection occurs close to the spacecraft. If protons are energized adiabatically while oxygen ions are energized non-adiabatically, then the two species will experience a spatial separation of the order of a gyroradius due to the electric field in the pickup process. In a 50 nT magnetic field, this separation will result in an average displacement of the O^+ ions on the order of 1 R_E. Therefore, in order to arrive at the spacecraft at the same time, the protons need to have higher energies. The measured energy shift would then depend on the ratio of the initial signal separation and the distance to the spacecraft. If the spacecraft is within several R_E of the injection site, then that original ~1 R_E displacement is significant. But an important aspect of this scenario is that the shift in energy for the O^+ ions does not immediately correspond to how much additional energy was initially put into the O^+, but instead depends on the distance to the injection site.

For Scenario #3 (Figure 11c), particles are again injected far from the spacecraft; however, they experience additional accerlation closer to spacecraft. In this scenario, O^+ energies can again appear to be substantially modified relative to the *E/q* ordering. Here the energy shift depends not only on the displacement towards the spacecraft caused by the injection, but equally on how much additional energy is added to the O^+ ions close to the spacecraft. Both effects (energy added to *E/q*-ordered behavior and spatial shifting) will play a role.

There are also other processes that we have not examined – e.g., the ion trapping process discussed by Ukhorskiy et al. (2017, 2018). We have also not considered Fermi-type processes whereby the sudden Earthward movement of curved field lines could add a velocity-based energy to heavier ions relative to light ions. We have examined the pitch angle dependence of the correlation traces and found that the correlation values of nearly parallel particles are substantially lower than those of perpendicular particles.

We conclude that the apparent mass-dependent energization seen in this analysis is a result of non-adiabatic energization processes such as those discussed here. However, interpreting that energization is very situation-dependent and will require substantial additional modeling to understand. We suspect that some of the observed events in the “indeterminate” category are the result of the complexities of the injection processes as only partially revealed in our examination of several potential scenarios (Figure 11). A possible approach for making further progress in the future would be to perform similar cross-correlation analyses on simulated distributions - e.g.,

500 those by Birn et al. (2021) and/or Ukhorsliy et al. (2018) - to see what kinds of patterns are
501 expected to emerge.

502 Ultimately, we conclude that the cross-correlation technique applied in this and previous studies
503 *can* be utilized to deduce the presence of different populations of ion species with different
504 charge states. However, the results are still rather limited in quantifying the energization
505 mechanism. The locations of the injection sites relative to the location of the spacecraft and the
506 possibility for the occurrence of multiple injections, will play a role in what the cross-
507 correlations between fluxes of different species will show. In cases of strong substorm activity
508 when the tail topology is highly dynamic and the particles go through numerous injections close
509 to the spacecraft, the temporal variation of fluxes associated with different species (including the
510 non-adiabatic behavior of O^+) will likely not be well ordered by *E/q*, and thus the cross-
511 correlations tables are unlikely to show ridges of high cross-correlations with clear boundaries.

512 **Acknowledgments**

513 The authors are grateful to the dedicated scientists and engineers of the MMS Science,
514 Instrument, and Operations Teams. Additional thanks are extended to Vassilis Angelopoulos,
515 Eric Grimes, and the teams at UCLA and Berkeley for their development and support of the
516 Space Physics Environment Data Analysis Software (SPEDAS) IDL framework (Angelopoulos
517 et al., 2019). The Level 2 data download and preprocessing for this work is performed within the
518 SPEDAS framework. This work was supported by the Magnetospheric Multiscale (MMS)
519 mission of NASA's Science Directorate Heliophysics Division via subcontract to the Southwest
520 Research Institute (NNG04EB99C).

521

522 **References**

523 Allen, R. C., S. A. Livi, S. K. Vines, and J. Goldstein (2016), Magnetic latitude dependence of
524 oxygen charge states in the global magnetosphere: Insights into solar wind-originating ion
525 injection, *J. Geophys. Res. Space Physics*, 121, 9888–9912, doi:10.1002/2016JA022925.

526 Allen, R. C., Livi, S. A., Vines, S. K., Goldstein, J., Cohen, I., Fuselier, S. A., et al. (2017).
527 Storm time empirical model of O^+ and O^{6+} distributions in the magnetosphere, *Journal of*
528 *Geophysical Research: Space Physics*, 122, 8353–8374. https://doi.org/10.1002/2017JA024245

529 Angelopoulos, V., Cruce, P., Drozdov, A., Grimes, E. W., Hatzigeorgiu, N., King, D. A., et al.
530 (2019). The space physics environment data analysis system (SPEDAS). *Space Science Reviews*,
531 215(1), 9. https://doi.org/10.1007/s11214-018-0576-4

532 Bingham, S. T., Cohen, I. J., Mauk, B. H., Turner, D. L., Mitchell, D. G., Vines, S. K., et al.
533 (2020). Charge-state-dependent energization of suprathermal ions during substorm injections
534 observed by MMS in the magnetotail. *Journal of Geophysical Research: Space Physics*, 125,
535 e2020JA028144. https://doi.org/10.1029/2020JA028144

536 Bingham, S. T., Nikoukar, R., Cohen, I. J., Mauk, B. H., Turner, D. L., Mitchell, D. G., et al.
537 (2021). Evidence for nonadiabatic oxygen energization in the near-Earth magnetotail from
538 MMS. *Geophysical Research Letters*, 48, e2020GL091697.
539 https://doi.org/10.1029/2020GL091697

540 Birn, J., M. Hesse, R. Nakamura, and S. Zaharia (2013), Particle acceleration in dipolarization
541 events, *J. Geophys. Res. Space Physics*, 118, 1960– 1971, doi:10.1002/jgra.50132.

542 Birn, J., A. Runov, and M. Hesse (2014), Energetic electrons in dipolarization events: Spatial
543 properties and anisotropy, *J. Geophys. Res. Space Physics*, 119, 3604– 3616,
544 doi:10.1002/2013JA019738.

545 Birn, J., Hesse, M., Bingham, S. T., Turner, D. L., & Nakamura, R. (2021). Acceleration of
546 oxygen ions in dipolarization events: 1. CPS distributions. *Journal of Geophysical Research:*
547 *Space Physics*, 126, e2021JA029184. https://doi.org/10.1029/2021JA029184

548 Blake, J. B., et al. (2016), The fly' eye energetic particle spectrometer (FEEPS) sensors for the
549 Magnetospheric Multiscale (MMS) mission, *Space Sci. Rev.*, 199(1), 309–329,
550 doi:10.1007/s11214-015-0163-x.

551 Burch, J. L., Moore, T. E., Torbert, R. B., & Giles, B. L. (2016). Magnetospheric multiscale
552 overview and science objectives. *Space Science Reviews*, 199(1–4), 5–21.
553 https://doi.org/10.1007/s11214-015-0164-9

554 Cohen, I. J., Mitchell, D. G., Kistler, L. M., Mauk, B. H., Anderson, B. J., Westlake, J. H., et al.
555 (2017). Dominance of high-energy (>150 keV) heavy ion intensities in Earth's middle to outer
556 magnetosphere, *Journal of Geophysical Research: Space Physics*, 122(9), 9282–9293.
557 https://doi.org/10.1002/2017JA024351

558 Daglis, I. A., and W. L. Axford (1996), Fast ionospheric response to enhanced activity in
559 geospace: Ion feeding of the inner magnetotail, *J. Geophys. Res*., 101, 5047–5065.

560 Delcourt, D. C., & Sauvaud, J. A. (1994). Plasma sheet ion energization during dipolarization
561 events, *Journal of Geophysical Research*, 99(A1), 97. https://doi.org/10.1029/93JA01895

562 Ebihara, Y. and Ejiri, M. (2003), Numerical Simulation of the Ring Current: Review, *Space*
563 *Science Reviews*, vol. 105, no. 1, pp. 377–452. doi:10.1023/A:1023905607888.

564 Fok, M.-C., T. E. Moore, P. C. Brandt, D. C. Delcourt, S. P. Slinker, and J. A. Fedder (2006),
565 Impulsive enhancements ofoxygen ions during substorms, *J. Geophys. Res.*,111, A10222,
566 doi:10.1029/2006JA011839

567 Fuselier, S.A., Lewis, W.S., Schiff, C. et al. (2016). Magnetospheric Multiscale Science Mission
568 Profile and Operations. *Space Sci Rev* 199, 77–103. https://doi.org/10.1007/s11214-014-0087-x

569 Gkioulidou, M., Ukhorskiy, A. Y., Mitchell, D. G., Sotirelis, T., Mauk, B. H., & Lanzerotti, L. J.
570 (2014). The role of small-scale ion injections in the buildup of Earth's ring current pressure: Van
571 Allen Probes observations of the 17 March 2013 storm, *Journal of Geophysical Research: Space*
572 *Physics*, 119(9), 7327–7342. https://doi.org/10.1002/2014JA020096

573 Gloeckler, G., & Hamilton, D. C. (1987). AMPTE ion composition results, *Physica Scripta*,
574 T18(T18), 73–84. https://doi.org/10.1088/0031-8949/1987/T18/009

575 Hamilton, D. C., G. Gloeckler, F. M. Ipavich, W. Studemann, B. Wilken, and G.
576 Kremser (1988), Ring current development during the great geomagnetic storm of February
577 86, *J. Geophys. Res.*, 93, 14,343–14,355.

578 Jordanova, V. K., Ilie, R., & Chen, M. W. (2020). *Ring current investigations: The quest for*
579 *space weather prediction*, Amsterdam, Netherlands: Elsevier.

580 Keika, K., P. C. Brandt, S. Ohtani, D. G. Mitchell, M. Nosé, T. Obara, H. Koshiishi, H.
581 Matsumoto (2010), Mass-dependent evolution of ENA energy spectra during stormtime

substorms: Implication for O+ nonadiabatic acceleration, *J. Geophys. Res.*, 115, A00I12, doi:10.1029/2010JA015889.

Keika, K., Kistler, L. M., & Brandt, P. C. (2013). Energization of O+ ions in the Earth's inner magnetosphere and the effects on ring current buildup: A review of previous observations and possible mechanisms, *Journal of Geophysical Research: Space Physics*, 118(7), 4441–4464. https://doi.org/10.1002/jgra.50371

Keika, K., Kasahara, S., Yokota, S., Hoshino, M., Seki, K., Nosé, M., et al. (2018). Ion energies dominating energy density in the inner magnetosphere: Spatial distributions and composition, observed by Arase/MEP-i. *Geophysical Research Letters*, 45 12153–12162. https://doi.org/10.1029/2018GL080047

King, J. H., & Papitashvili, N. E. (2005). Solar wind spatial scales in and comparisons of hourly wind and ACE plasma and magnetic field data. *Journal of Geophysical Research*, 110(A2), A02104. https://doi.org/10.1029/2004JA010649

Kistler, L. M., Ipavich, F. M., Hamilton, D. C., Gloeckler, G., Wilken, B., Kremser, G., & Stüdemann, W. (1989), Energy spectra of the major ion species in the ring current during geomagnetic storms, *Journal of Geophysical Research*, 94(A4), 3579–3599. https://doi.org/10.1029/JA094iA04p03579

Kistler, L. M., M bius, E., Klecker, B., Gloeckler, G., Ipavich, F. M., & Hamilton, D. C. (1990). Spatial variations in the suprathermal ion distributions during substorms in the plasma sheet, *Journal of Geophysical Research*, 95(A11), 18871. https://doi.org/10.1029/JA095iA11p18871

Kozyra, J.U. and Liemohn, M.W. (2003), Ring Current Energy Input and Decay, *Space Science Reviews*, 109, 105–131. https://doi.org/10.1023/B:SPAC.0000007516.10433.ad

Kremser, G., W. Stridemann, B. Wilken, G. Gloeckler, D.C. Hamilton, F. M. Ipavich, and D. Hovestadt (1985), Charge state distributions of oxygen and carbon in the energy range 1 to 300 keV/e observed with AMPTE/CCE in the magnetosphere, *Geophys. Res. Lett.*, 12, 847.

Kremser, G., Stüdemann, W., Wilken, B., Gloeckler, G., Hamilton, D. C., & Ipavich, F. M. (1987). Average spatial distributions of energetic O^+ , O^{2+} , O^{6+} , and C^{6+} ions in the magnetosphere observed by AMPTE CCE. *Journal of Geophysical Research*, 92(A5), 4459. https://doi.org/10.1029/JA092iA05p04459

Kronberg, E. A., et al. (2014), Circulation of heavy ions and their dynamical effects in the magnetosphere: Recent observations and models, *Space Sci. Rev.*, 184(1-4), 173–235, doi:10.1007/s11214-014-0104-0.

Mauk, B. H. (2013), Analysis of EMIC-wave-moderated flux limitation of measured energetic ion spectra in multispecies magnetospheric plasmas, *Geophys. Res. Lett.*, 40, 3804–3808, doi:10.1002/grl.50789.

Mauk, B. H. (2016), The Energetic Particle Detector (EPD) Investigation and the energetic ion spectrometer (EIS) for the magnetospheric multiscale (MMS) mission, *Space Science Reviews*, 199(1–4), 471–514. https://doi.org/10.1007/s11214-014-0055-5

Mitchell, D. G., Gkioulidou, M., & Ukhorskiy, A. Y. (2018). Energetic ion injections inside geosynchronous orbit: Convection- and drift-dominated, charge-dependent Adiabatic

energization (W = qEd). Journal of Geophysical Research: Space Physics, 123(8), 6360–6382. https://doi.org/10.1029/2018JA025556

Mobius, E., Scholer, M., Klecker, B., Hovestadt, D., Gloeckler, G., & Ipavich, F. M. (1987). Acceleration of ions of ionospheric origin in the plasma sheet during substorm activity. In A. T. Y. Lui (Ed.), *Magnetotail physics* (Vol. 20, pp. 231–234). Baltimore, MD: John Hopkins Univ. Press.

Moore, T. E., M. O. Chandler, M.-C. Fok, B. L. Giles, D. C. Delcourt, J. L. Horwitz, and C. J. Pollock (2001), Ring current and internal plasma sources, *Space Sci. Rev.*, 95, 555–568.

Mouikis, C. G., Bingham, S. T., Kistler, L. M., Farrugia, C. J., Spence, H. E., Reeves, G. D., et al. (2019). The storm-time ring current response to ICMEs and CIRs using Van Allen Probe observations, *Journal of Geophysical Research: Space Physics*, 124, 9017–9039. https://doi.org/10.1029/2019JA026695

Nakamura, R., et al. (2002), Motion of the dipolarization front during a flow burst event observed by Cluster, *Geophys. Res. Lett.*, 29(20), 1942, doi:10.1029/2002GL015763.

Nosé, M., Ohtani, S., Takahashi, K., Lui, A. T. Y., McEntire, R. W., Williams, D. J., et al. (2001). Ion composition of the near-Earth plasma sheet in storm and quiet intervals: Geotail/EPIC measurements, *Journal of Geophysical Research*, 106(A5), 8391–8403. https://doi.org/10.1029/2000ja000376

Nosé, M., H. Koshiishi, H. Matsumoto, P. C. son Brandt, K. Keika, K. Koga, T. Goka, and T. Obara (2010), Magnetic field dipolarization in the deep inner magnetosphere and its role in development of O+-rich ring current, *J. Geophys. Res*., 115, A00J03, doi:10.1029/2010JA015321.

Ono, Y., Nosé, M., Christon, S. P., & Lui, A. T. Y. (2009). The role of magnetic field fluctuations in non-adiabatic acceleration of ions during depolarization, *Journal of Geophysical Research*, 114(5), 1–11. https://doi.org/10.1029/2008JA013918

Pollock, C., Moore, T., Jacques, A., Burch, J., Gliese, U., Saito, Y., et al. (2016). Fast plasma investigation for magnetospheric multiscale, Space Science Reviews, 199(1–4), 331–406. https://doi.org/10.1007/s11214-016-0245-4

Roeder, J. L., J. F. Fennell, M. W. Chen, M. Schulz, M. Grande, and S. Livi (1996), CRRES observations of the composition of the ring-current ion populations, *Adv. Space Res.,* 17(10), 17–24.

Russell, C. T., Anderson, B. J., Baumjohann, W., Bromund, K. R., Dearborn, D., Fischer, D., et al. (2016). The magnetospheric multiscale magnetometers. *Space Science Reviews*, 199(1–4), 189–256. https://doi.org/10.1007/s11214-014-0057-3

Sanchez, E. R., Mauk, B. H., & Meng, C.-I. (1993). Adiabatic vs. non-adiabatic particle distributions during convection surges, *Geophysical Research Letters*, 20(3), 177–180. https://doi.org/10.1029/93GL00237

Sergeev, V., V. Angelopoulos, S. Apatenkov, J. Bonnell, R. Ergun, R. Nakamura, J. McFadden, D. Larson, and A. Runov (2009), Kinetic structure of the sharp injection/dipolarization front in the flow-braking region, *Geophys. Res. Lett.*, 36, L21105, doi:10.1029/2009GL040658.

664 Shelley, E. G., Johnson, R. G., & Sharp, R. D. (1972). Satellite observations of energetic heavy
665 ions during a geomagnetic storm, *Journal of Geophysical Research*, 77(31), 6104–6110.
666 https://doi.org/10.1029/JA077i031p06104

667 Thorne, R. M., and R. B. Horne (1997), Modulation of electromagnetic ion cyclotron instability
668 due to interaction with ring current O+ during magnetic storms, *J. Geophys.*
669 *Res.*, 102(A7), 14,155–14,163, doi:10.1029/96JA04019.

670 Ukhorskiy, A. Y., M. I. Sitnov, V. G. Merkin, M. Gkioulidou, and D. G. Mitchell (2017), Ion
671 acceleration at dipolarization fronts in the inner magnetosphere, J. Geophys. Res. Space Physics,
672 122, 3040–3054, doi:10.1002/2016JA023304.

673 Ukhorskiy, A. Y., Sorathia, K. A., Merkin, V. G., Sitnov, M. I., Mitchell, D. G., & Gkioulidou,
674 M. (2018). Ion trapping and acceleration at dipolarization fronts: High-resolution MHD and test-
675 particle simulations. Journal of Geophysical Research: Space Physics, 123, 5580–5589.
676 https://doi.org/10.1029/2018JA025370

677 Welling, D. T., Andr , M., Dandouras, I., Delcourt, D., Fazakerley, A., Fontaine, D., et al.
678 (2015), The Earth: Plasma sources, losses, and transport processes, *Space Science Reviews*,
679 192(1–4), 145–208. https://doi.org/10.1007/s11214-015-0187-2

680 Williams, D. J. (1985), Dynamics of the earth's ring current: theory and observation., *Space*
681 *Science Reviews*, vol. 42, no. 3–4, pp. 375–396, 1985. doi:10.1007/BF00214994.

682 Wygant, J., D. Rowland, H. J. Singer, M. Temerin, F. Mozer, and M. K.
683 Hudson (1998), Experimental evidence on the role of the large spatial scale electric field in
684 creating the ring current*, J. Geophys. Res.*, 103(A12), 29,527–29,544, doi:10.1029/98JA01436.

685 Yang, B., Q. G. Zong, S. Y. Fu, X. Li, A. Korth, H. S. Fu, C. Yue, and H. Rème (2011), The role
686 of ULF waves interacting with oxygen ions at the outer ring current during storm times, *J.*
687 *Geophys. Res.*, 116, A01203, doi:10.1029/2010JA015683.

688 Young, D.T., Balsiger, H., & Geiss, J. (1982). Correlations of magnetospheric ion composition
689 with geomagnetic and solar activity. *Journal of Geophysical Research, 87*, 9077-9096.

690 Ziegler, J. F., M. D. Ziegler, and J. P. Biersack (2010), SRIM—The stopping and range of ions
691 in matter (2010), *Nucl. Instrum. Methods Phys. Res.*, Sect. B, 268(11-12), 1818–1823,
692 doi:10.1016/j.nimb.2010.02.091.

693
694

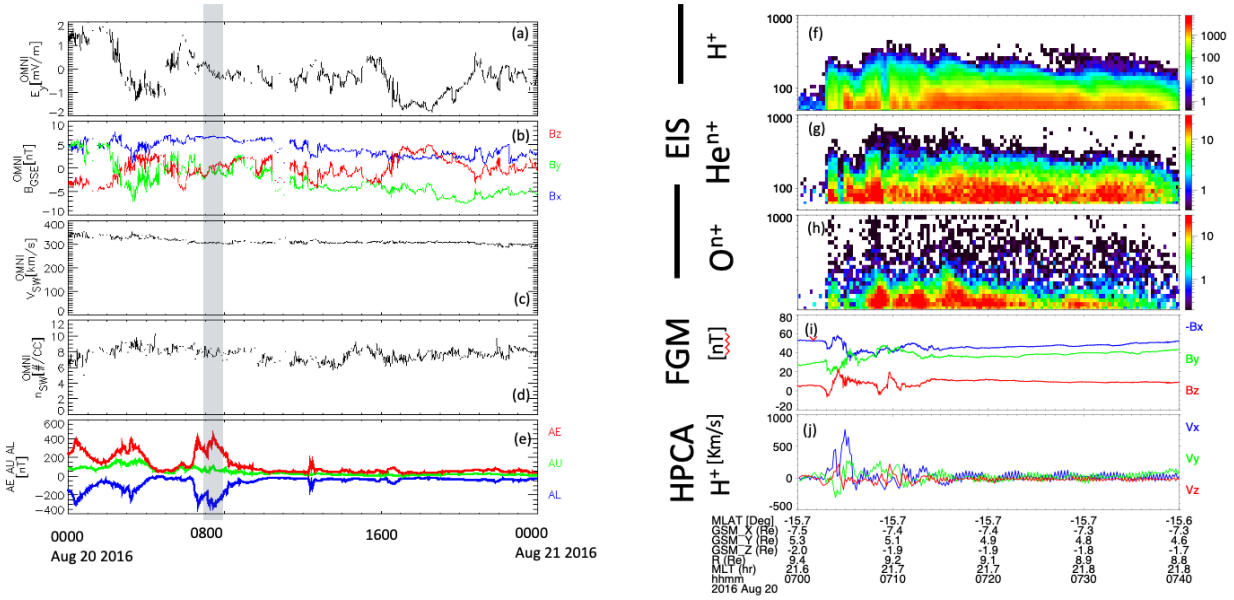

Figure 1. The first example case presented in this study: an energetic particle enhancement event observed by MMS on 20 August 2016 between 07:00 – 07:40 UT. OMNI solar wind conditions (a-d), substorm auroral indices (e), energy spectrograms of EIS ExTOF hydrogen, helium, and oxygen (f-h), FGM magnetic field measurements (i) and HPCA ion speed (j). This enhancement event occurs during moderate substorm activity, and is accompanied by dipolarization of the magnetic field and high plasma flows. The gray-shaded region notes the time interval associated with the event.

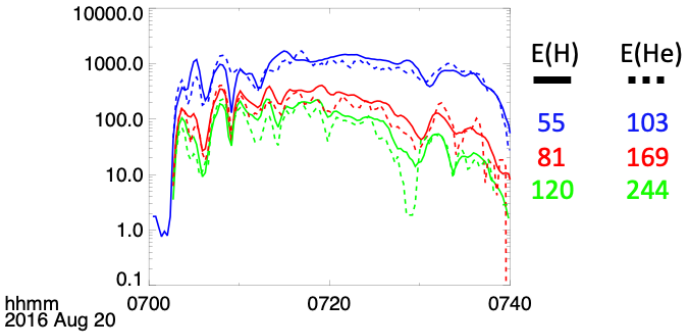

Figure 2. Time series of protons (solid) and helium (dashed) fluxes at various energies during the event on 20 August 2016 from 07:00-07:40 UT. Different colors correspond to different sets of energies as noted on the side of the figure. The time series of protons and helium fluxes (at twice the proton energies) show a similar behavior, and thus we expect to have a high correlation coefficient between these time series.

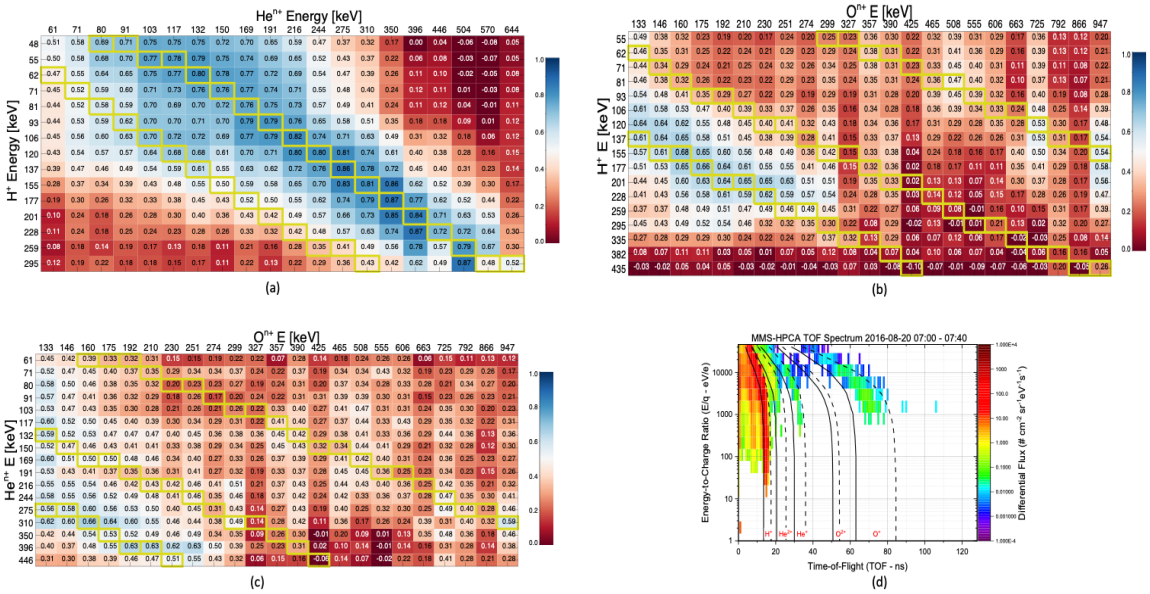

Figure 3. Tables showing cross-correlation coefficients between different species across energies for the enhancement event on 20 August 2016; cross-correlations are computed for 7:06 UT and 7:40 UT to avoid the high plasma flows observed by HPCA. a) Protons versus helium with a ridge of high correlation coefficients along $E_{He} = 2 * E_{H^+}$ indicating adiabatic energization of He^{++}. b) Protons versus oxygen with two ridges of high correlations along $E_O = E_{H^+}$ and $E_O = 6 * E_{H^+}$ indicating adiabatic energization of O^+ and O^{6+}. c) Helium versus oxygen with two ridges of higher cross-correlation coefficients along $E_O = \frac{1}{2} E_{He}$ and $E_O = 3 * E_{H^+}$. d) HPCA time-of-flight spectrum for the same time.

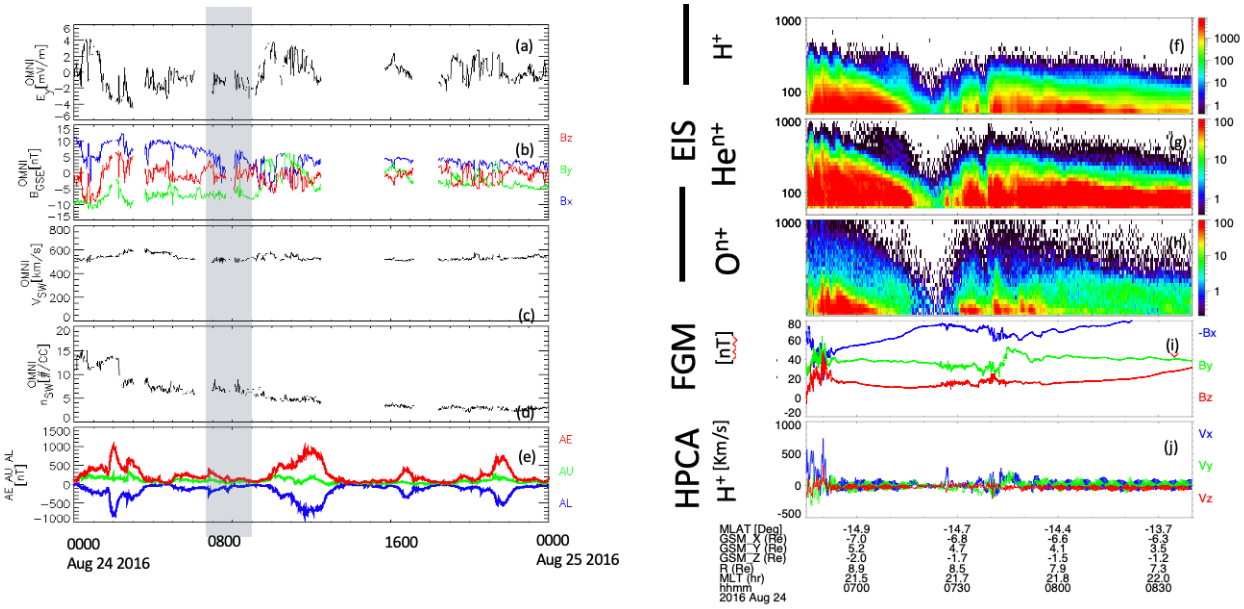

Figure 4. The second example case presented in this study: an energetic particle enhancement event observed by MMS on 24 August 2016 between 06:45 – 07:40 UT. OMNI solar wind conditions (a-d), substorm auroral indices (e), energy spectrograms of EIS ExTOF hydrogen, helium, and oxygen (f-h), FGM magnetic field measurements (i) and HPCA ion speed (j). This enhancement event occurs during moderate/weak substorm activity, and is accompanied by dipolarization of the magnetic field and high (~600 km/s) plasma flows at the beginning of the interval. The gray-shaded region notes the time interval associated with the event.

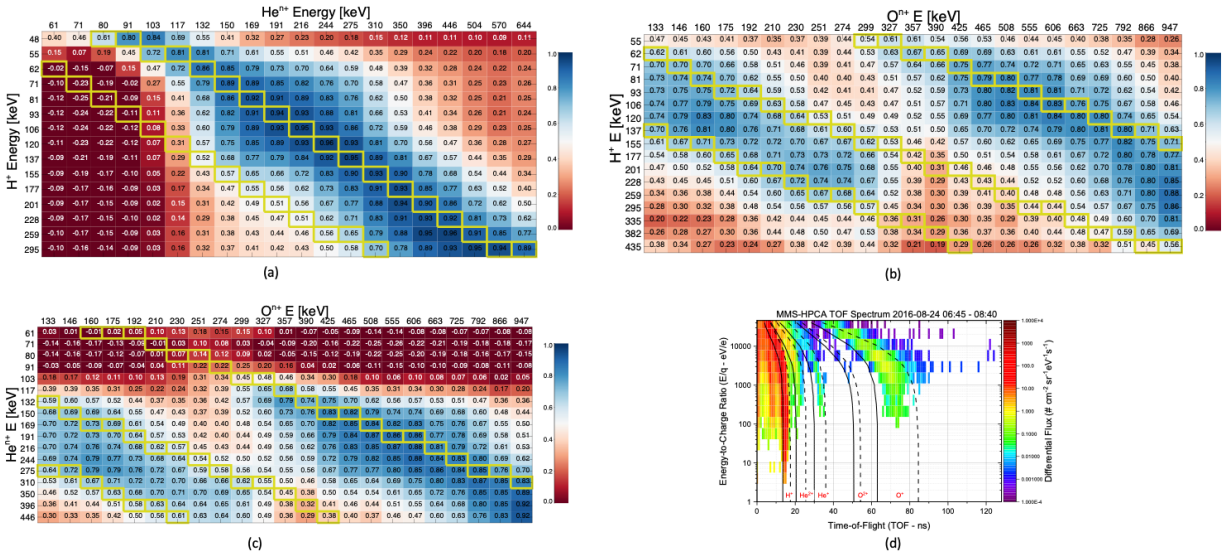

Figure 5. Cross-correlation coefficients between different species at various energies for the enhancement event on 24 August 2016; cross-correlations are computed from 6:50-8:45 UT to avoid the high plasma flows observed in HPCA flow measurements. a) Protons versus helium with a ridge of high correlation coefficients along $E_{He} = 2 * E_{H^+}$ indicating adiabatic energization of He^{++}. b) Protons versus oxygen with a strong ridge of high correlation along $E_O = 6 * E_{H^+}$ for E_O>~300 keV indicating adiabatic energization of O^{6+}. Another strong ridge of high correlation is evident for lower energy oxygen that lies between $E_O = E_{H^+}$ and $E_O = 2 * E_{H^+}$.c) Helium versus oxygen with two ridges of higher cross-correlation coefficients: one along $E_O = 3 * E_{He}$ and another one between $E_O = \frac{1}{2} * E_{He}$ and $E_O = E_{He}$. d) HPCA TOF spectrum for the same time interval.

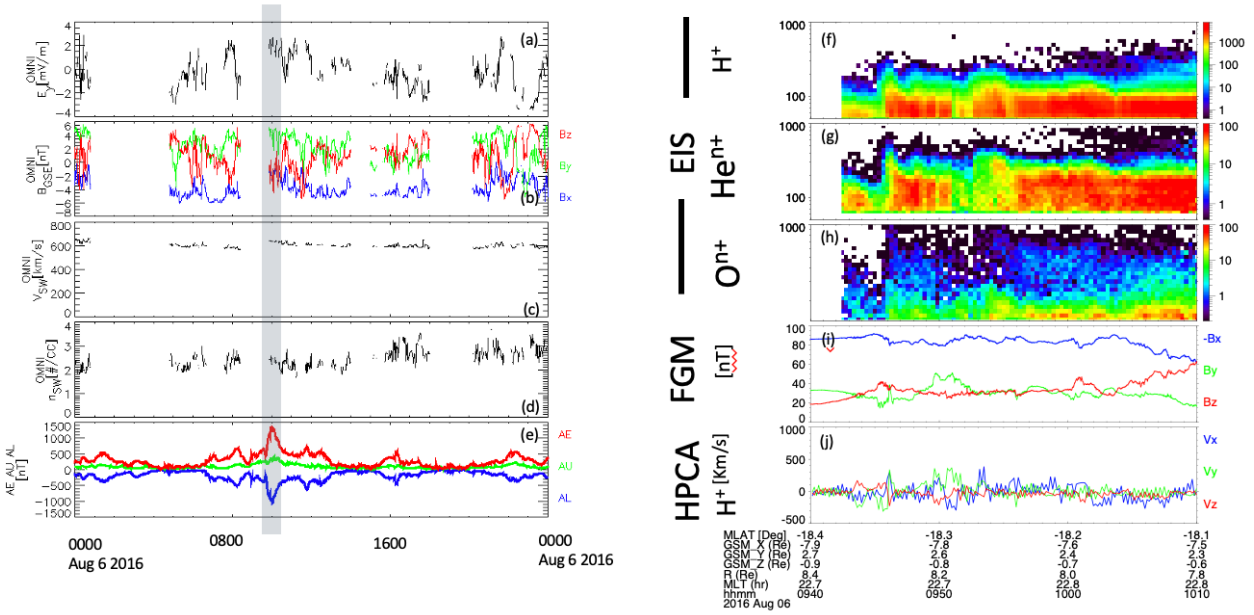

Figure 6. The third example case presented in this study: an energetic particle enhancement event as observed by MMS on 6 August 2016 between 09:40 – 10:10 UT. OMNI solar wind conditions (a-d), substorm auroral indices (e), spectrograms of EIS ExTOF hydrogen, helium, and oxygen (f-h), FGM magnetic field measurements (i) and HPCA ion speed (j). This enhancement event occurs during strong substorm activity, and is accompanied by dipolarization of the magnetic field throughout the interval. The gray-shaded region notes the time interval associated with the event.

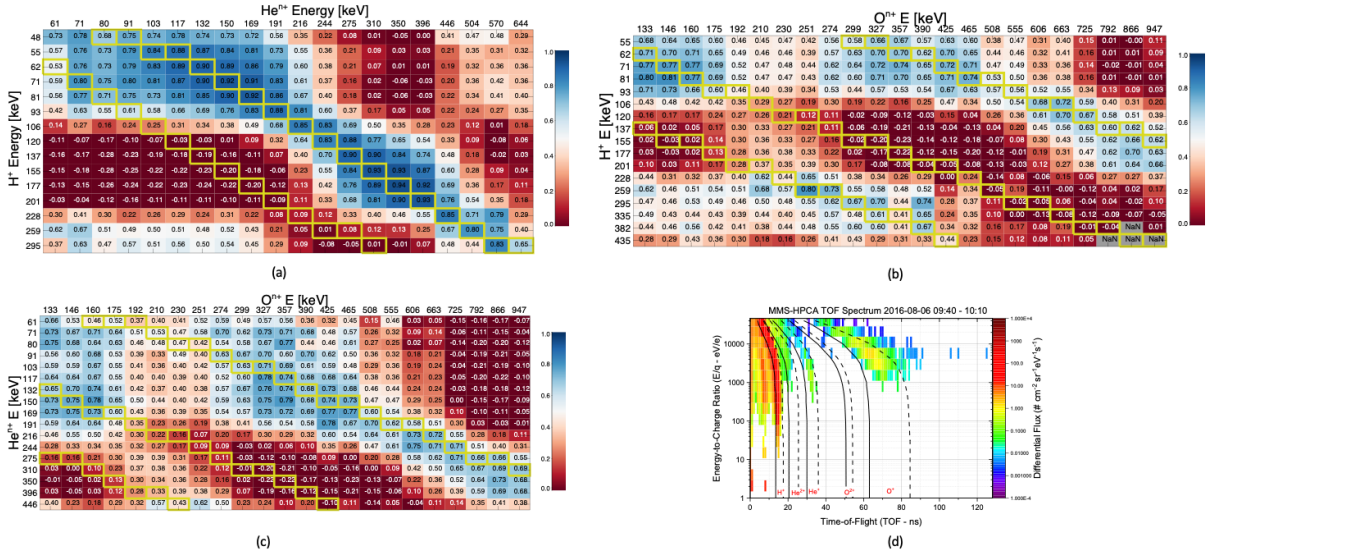

Figure 7. Cross-correlation coefficients between different species at various energies for the enhancement event on 6 August 2016 between 9:40 UT and 10:10 UT. a) Protons versus helium with a ridge of high correlation coefficients along $E_{He} = 2 * E_{H^+}$ indicating adiabatic energization of He^{++}. b) Protons versus oxygen with a strong ridge of high correlation along $E_O = 6 * E_{H^+}$ for E_O>~300 keV indicating adiabatic energization of O^{6+}. Two other ridges of high correlations are shown along $E_o = 2 * E_{H^+}$ and another one along and below $E_O = E_{H^+}$ line. c) Helium versus oxygen with two ridges of higher cross-correlation coefficients: one along $E_O = 3 * E_{He}$ and another one between $E_O = \frac{1}{2} * E_{He}$ and $E_O = 3 * E_{He}$. d) HPCA TOF spectrum for the same time interval.

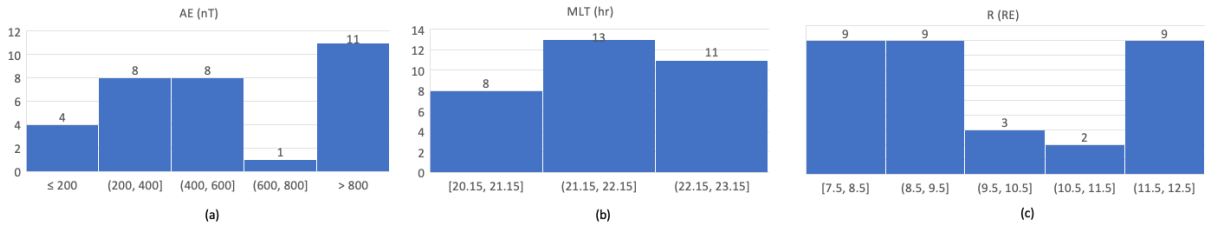

Figure 8. The histograms of the enhancement events in terms of substorm activity (auroral electrojet index AE) in (a), MLT distribution of the events in (b), and radial distance from the center of the Earth in (c).

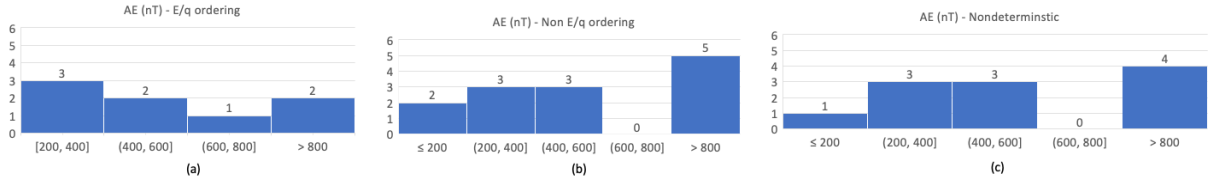

Figure 9. Histograms of the identified energetic ion enhancement events versus substorm activity (auroral electrojet index, AE) for the different categories: a) adiabatic energization of O^+, b) non-adiabatic energization of O^+, and c) inconclusive in terms of O^+ energization behavior.

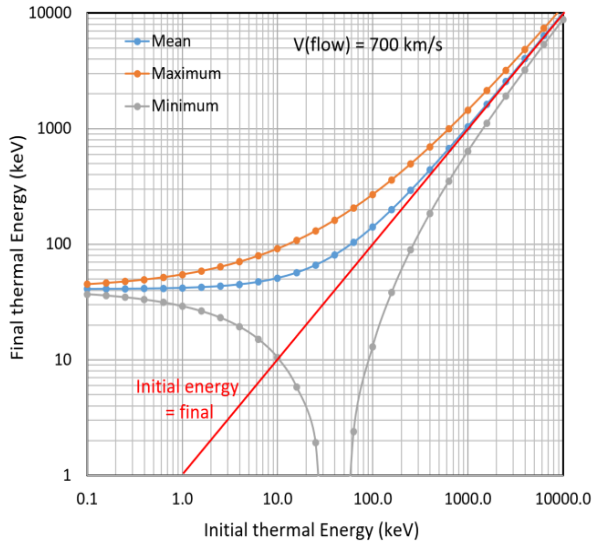

Figure 10. A preliminary approach to illustrate the "pick-up" process that occurs when a very strong electric field is turned on at a rate much faster than the ion gyroperiod. One interpretation of the correlation shift observed by Bingham et al. (2021) was based on the mean blue trace in this figure. However, the orange and grey lines show the maximum and minimum energies that can be achieved by ions with a distribution of initial gyrophases.

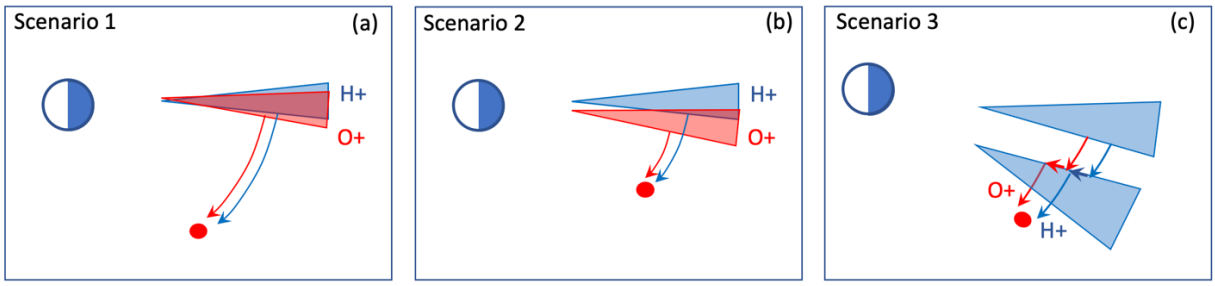

Figure 11. Three different scenarios depicting the relative location of spacecraft and the injection site.